AIAA JOURNAL
Vol. 47, No. 2, February 2009

Implicit Nonlinear Frequency-Domain Spectral-Difference Scheme for Periodic Euler Flow

Jean-Sebastien Cagnone* and Siva K. Nadarajah†
McGill University, Montreal, Quebec H3A 2S6, Canada

DOI: 10.2514/1.37978

This paper combines a nonlinear frequency-domain scheme with a high-order spectral-difference discretization for the two-dimensional unsteady Euler equations. An implicit lower/upper symmetric Gauss–Seidel method is introduced to solve the nonlinear frequency-domain equations. High-order accuracy and solution acceleration due to the implicit treatment are numerically verified on the vortex advection and subsonic airfoil test cases. Finally, the performance of this implicit high-order scheme on a fully compact stencil for periodic flows is evaluated on a pitching-airfoil problem.

Nomenclature

b	=	mesh velocity
c	=	airfoil chord
c_l	=	lift coefficient
c_p	=	pressure coefficient
$\mathbf{F}$	=	flux vector
$\mathbf{f}$, $\mathbf{g}$	=	flux vector
h, l	=	Lagrange polynomials
k	=	wave number
M	=	Mach number
n	=	time level
p	=	pressure
R	=	residual
$\hat{R}$	=	Fourier coefficient of residual
T	=	temperature
t	=	time
u, v	=	velocity components
w	=	state vector
$\hat{w}$	=	Fourier coefficient of the state vector
x, y	=	coordinates (physical domain)
α	=	angle of attack
γ	=	specific heats ratio
ε	=	vortex strength
ξ, η	=	coordinates (computational domain)
ρ	=	density
τ	=	pseudotime
ϕ	=	solution shape function
φ, ψ	=	flux shape function
χ_s	=	solution point coordinate
$\chi_{s+1/2}$	=	flux point coordinate
ω_r	=	reduced frequency

I. Introduction

SIMULATION of periodic flows using a time-accurate integration scheme is a costly procedure. One needs to select a time step such that the flow physics are well captured and then integrate in time until a periodic steady state is achieved. Most of the computational resources are thus spent on resolving the initial transient before obtaining the sought periodic steady state. Moreover, if the flow phenomena have complex features that only very fine grids can resolve, then the prohibitive cost of each time step may lead to computational times that are unacceptable for practical engineering applications. Notably, vortical flow over multi-element airfoils, leading-edge vortex shedding, and flutter conditions remain very challenging cases due to the highly nonlinear unsteady viscous effects. Rotorcraft aerodynamics also present similar complexities in which each blade's wake influences the next, leading to intricate blade–vortex and shock–vortex interactions. Although these cases have already been tackled successfully, they represent the state of the art in aerospace computational fluid dynamics and would benefit from more efficient solution techniques.

To reduce the computational effort associated with periodic simulations, Hall et al. [1] first proposed the harmonic balance technique in the context of turbomachinery flow analysis. The method hinges on a linearized pseudospectral transformation of the governing equations to the Fourier space in which they are solved for a given number of harmonics. McMullen et al. [2,3] later extended the technique to include the nonlinear effects, giving rise to the present nonlinear frequency-domain (NLFD) method. Since then, Nadarajah [4] proved that this method fully accounts for strong linearity and exhibits spectral-like convergence even for viscous flows with moving shocks. Gopinath and Jameson [5] contributed the time-spectral method, in which each time instance is solved in real space, and the solution's periodicity is imposed trough a premultiplied Fourier collocation matrix.

Although much effort has been devoted to refining the temporal representation of periodic flows, the spatial discretization in the NLFD technique has received comparatively little attention. Although the prevailing second-order-accurate finite volume methods are very well suited for mainstream usage, most of the aforementioned applications require high-order numerical techniques to accurately describe the flow features. With this intent, we propose to trade the low-order discretization that has been used with the NLFD method for the spectral-difference method, thereby achieving the required flow resolution.

Difference schemes using cellwise-staggered polynomials were pioneered by Kopriva and Kolias [6] and Kopriva [7] as the staggered-grid multidomain method for structured grids. In a later effort, Liu et al. [8] applied similar concepts and developed the spectral-difference (SD) scheme for unstructured tetrahedral grids in an attempt to create a more efficient spectral-volume scheme. The extension of the SD scheme to the Euler and Navier–Stokes equations was established by Wang and Liu [9], Sun et al. [10], and May and Jameson [11]. The SD scheme is a conservative, high-order, efficient method for conservation laws, comparable with the discontinuous Galerkin (DG) [12,13] and spectral-volume (SV) [14,15] schemes. Similarities between the SD scheme and DG and

Received 9 April 2008; revision received 13 November 2008; accepted for publication 20 October 2008.

*Graduate Student, Department of Mechanical Engineering. Student Member AIAA.
†Assistant Professor, Department of Mechanical Engineering. Member AIAA.

SV methods have been drawn by Huynh [16] and Van den Abeele et al. [17], respectively. As for those discretization techniques, the spectral difference achieves high order by locally approximating the solution as a high-degree polynomial inside each cell. However, being based on the differential form of the equations, its formulation is simpler than that of the DG and SV methods, as no test function or quadrature is involved. Conservation properties are still maintained by a judicious placement of the nodes at quadrature points of the chosen simplex. Recently, Van den Abeele et al. [18] explored alternative SD schemes, modifying the basis functions to give rise to a family of SD formulations for structured and unstructured grids. These researchers showed that a broad class of staggering and nonstaggering node placements are possible.

This paper proposes the complete nonlinear frequency-domain/spectral-difference (NLFD-SD) scheme for the Euler equations. The framework is independent of the spatial discretization retained and is applicable to all SD formulations as described by Van den Abeele et al. [18], including the original staggered-grid multidomain method of Kopriva and Kolias [6] and Kopriva [7] and the unstructured SD of Liu et al. [8]. In this work, quadrilateral cells are considered and the staggered-grid multidomain approach is therefore employed. Two novel ideas are brought forward: 1) the use of spectral time representation in conjunction with a high-order spatial discretization and 2) the implicit lower/upper symmetric Gauss–Seidel (LU-SGS) treatment of the resulting set of equations. Section II gives a brief review of the spectral-difference method then discusses the NLFD technique, focusing on the implicit solution strategy. Section III presents a complete numerical validation of the spatial and temporal discretizations on the vortex advection and subsonic NACA0012 test cases. Finally, a pitching NACA64A010 simulation is demonstrated as a test case for the developed scheme.

II. Formulation of the NLFD Spectral-Difference Method

A. Governing Equations

Consider the unsteady 2-D Euler equations in conservative form:

$$\frac{\partial \mathbf{w}}{\partial t} + \nabla \cdot \mathbf{F} = 0 \tag{1}$$

where $\mathbf{w}$ is the vector of conserved variables and $\mathbf{F} = (\mathbf{f}, \mathbf{g})$ are the inviscid flux vectors, respectively. They are given by

$$\mathbf{w} = \begin{Bmatrix} \rho \\ \rho u \\ \rho v \\ \rho E \end{Bmatrix}, \qquad \mathbf{f} = \begin{Bmatrix} \rho(u-b_x) & \\ \rho u(u-b_x) & +p \\ \rho v(u-b_x) & \\ \rho E(u-b_x) & +pu \end{Bmatrix}$$
$$\mathbf{g} = \begin{Bmatrix} \rho(v-b_y) & \\ \rho u(v-b_y) & \\ \rho v(v-b_y) & +p \\ \rho E(v-b_y) & +pv \end{Bmatrix} \tag{2}$$

In these definitions, ρ is the density, b_x and b_y are Cartesian velocity components of the boundary, E is the total energy, and p is the pressure determined by the equation of state:

$$p = (\gamma - 1)\rho\{E - \tfrac{1}{2}(u^2 + v^2)\}$$

with a constant ratio of specific heats $\gamma = 1.4$ for air.

B. Spatial Discretization

The basis for the spectral-difference solver of order k is a superposition of two grids within each computational cell. Their arrangement within the reference element spanning

$$(\xi, \eta) \in [-1, 1] \times [-1, 1]$$

is illustrated in Fig. 1. This particular choice corresponds to the Chebysev–Gauss–Lobatto basis, and the staggered-grid multidomain formulation of Kopriva and Kolias [6] and Kopriva [7] is

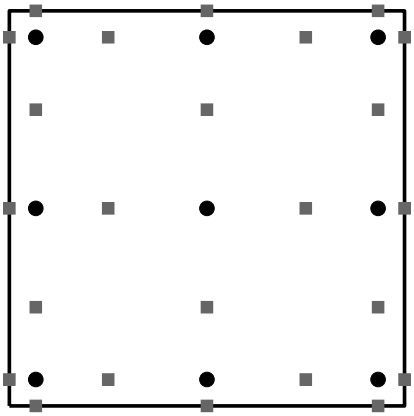

Fig. 1 Solution (●) and fluxes (■) grid for the third-order SD scheme.

recovered. The first grid holds the conserved variables and is chosen such that a polynomial solution of degree $k-1$ may be supported. The coordinates of those so-called *solution points* are given by the Gauss–Chebyschev quadrature points:

$$\chi_s = \cos\left(\pi \frac{2s-1}{2k}\right), \qquad s = 1, 2, \ldots, k \tag{3}$$

Similarly, the fluxes are reconstructed on a second grid supporting a polynomial of degree k. Those *flux points* are given by the Gauss–Lobatto points:

$$\chi_{s+1/2} = \cos\left(\pi \frac{s}{k}\right), \qquad s = 0, 1, \ldots, k \tag{4}$$

Once the nodal placement is defined, Lagrange polynomials are introduced to create an interpolation basis:

$$h_i(\chi) = \prod_{s=1, s\neq i}^{k} \left(\frac{\chi - \chi_s}{\chi_i - \chi_s}\right)$$
$$l_{i+1/2}(\chi) = \prod_{s=0, s\neq i}^{k} \left(\frac{\chi - \chi_{s+1/2}}{\chi_{i+1/2} - \chi_{s+1/2}}\right) \tag{5}$$

The product of those Lagrange polynomials in each spatial direction defines the shape functions used to interpolate the solution using the discrete nodal values:

$$w(\xi, \eta) = \{\phi\}^T\{w\}$$
$$\phi_{i,j}(\xi, \eta) = h_i(\xi) \cdot h_j(\eta), \qquad (\xi, \eta) \in [-1, 1] \tag{6}$$

The shape functions for the fluxes interpolation are defined similarly:

$$\varphi_{i,j}(\xi, \eta) = l_{i+1/2}(\xi) \cdot h_j(\eta)$$
$$\psi_{i,j}(\xi, \eta) = h_i(\xi) \cdot l_{j+1/2}(\eta), \qquad (\xi, \eta) \in [-1, 1] \tag{7}$$

An evaluation of the residual is done in two steps. First, the conserved variables are interpolated to each flux point. At the inner points, the solution is continuous and the analytical flux vector is evaluated. At the boundary of the computational cell, the solution is allowed to be discontinuous, and a Riemann solver is required to retrieve a stable single-valued normal flux. Our unsteady simulations use the Rusanov [19] flux for its simplicity and low computational cost. For the steady cases, the Roe [20] flux is used to promote accuracy:

$$f_{\text{Rusanov}} = \tfrac{1}{2}[f_L + f_R - (|v_n - b| + c)(w_R - w_L)] \tag{8}$$

$$f_{\text{Roe}} = \tfrac{1}{2}[f_L + f_R - R|\Lambda|R^{-1}(w_R - w_L)] \tag{9}$$

where c is the speed of sound, b is the mesh velocity, R is the eigenvector matrix, and $|\Lambda|$ is the entropy-fixed absolute

eigenvalues. The analytical tangential flux is also evaluated locally and is kept discontinuous across each face.

Second, once the full flux vector is known at each flux point, the divergence of the fluxes are computed at the solution points. Applying the chain rule, we can obtain the divergence of the fluxes in physical space using the appropriate metric terms

$$\nabla \cdot \mathbf{F} = \frac{\partial f}{\partial \xi}\xi_x + \frac{\partial f}{\partial \eta}\eta_x + \frac{\partial g}{\partial \xi}\xi_y + \frac{\partial g}{\partial \eta}\eta_y \tag{10}$$

or, in terms of the discrete nodal values,

$$\nabla \cdot \mathbf{F} = \xi_x\{\varphi_\xi\}^T\{f\} + \eta_x\{\psi_\eta\}^T\{f\} + \xi_y\{\varphi_\xi\}^T\{g\} + \eta_y\{\psi_\eta\}^T\{g\} \tag{11}$$

In accordance with the method of lines, our discretization results in a set of ordinary differential equations to which the time-integration scheme will be applied:

$$\frac{\partial w}{\partial t} + R(w) = 0 \tag{12}$$

For an in-depth description of the spectral difference on quadrilateral cells, the reader is referred to the work of Sun et al. [10].

It is well known that high-order methods require special representation of curved boundaries [11,21,22]. For that purpose, cells with quadratic edges are used to accommodate the curvature of the solid walls to be treated. This is realized by adding a node to each segment representing a curved edge, then using the resulting high-order metrics. In this research, this additional node is obtained through a globally interpolated B-spline. Bassi and Rebay [21] report that the improvement due to high-order boundaries is mainly related to the correct distribution of the normal vectors. To take this into account, the normal vectors are computed from the analytical derivatives of the fitted B-spline. In this paper, all the airfoil simulations have benefited from this high-order-boundary approach.

C. Temporal Discretization

With the equations cast in semidiscrete form, we now turn our attention to the temporal discretization. If a time-accurate strategy is chosen, then the solution may be directly integrated forward in time using standard explicit or implicit techniques. Here, we favor a time-spectral approach in which the periodicity of the state and residual vectors is assumed. Consequently, w and R may be represented by separate Fourier series:

$$w = \sum_{k=-\frac{N}{2}}^{\frac{N}{2}} \hat{w}\, e^{ikt}, \qquad R = \sum_{k=-\frac{N}{2}}^{\frac{N}{2}} \hat{R}\, e^{ikt} \tag{13}$$

where $i = \sqrt{-1}$. Those expressions are replaced in Eq. (12), and using the orthogonality property of the Fourier series yields a separate equation for each wave number:

$$ik\hat{w}_k + \hat{R}_k = 0 \tag{14}$$

To solve the preceding equation, a pseudotime derivative is added, and the resulting equations are integrated to steady state, at which point Eq. (14) is satisfied:

$$\frac{d\hat{w}_k}{d\tau} + ik\hat{w}_k + \hat{R}_k = 0 \tag{15}$$

Further details on the NLFD scheme and its implementation are provided by McMullen et al. [2,3] and McMullen [23] and will not be repeated here. In those references, the integration to steady state is done using a multistage Runge–Kutta method. For the sake of comparison, we have employed the following five-stage scheme [24] :

$$\begin{aligned}
\hat{w}_k^0 &= \hat{w}_k^n \\
\hat{w}_k^1 &= \hat{w}_k^n + \alpha_1 \Delta\tau \hat{R}(\hat{w}_k^0)^\star \\
&\vdots \\
\hat{w}_k^5 &= \hat{w}_k^n + \alpha_5 \Delta\tau \hat{R}(\hat{w}_k^4)^\star \\
\hat{w}_k^{n+1} &= \hat{w}_k^5
\end{aligned} \tag{16}$$

where $\hat{R}(\hat{w})^\star = -ik\hat{w}_k - \hat{R}_k$, and the coefficients are given by

$$\alpha_1 = \tfrac{1}{4}, \qquad \alpha_2 = \tfrac{1}{6}, \qquad \alpha_3 = \tfrac{3}{8}, \qquad \alpha_4 = \tfrac{1}{2}, \qquad \alpha_5 = 1 \tag{17}$$

However, greater efficiency may be obtained using an implicit technique. For that purpose, we introduce an implicit LU-SGS method adapted from the work of Sun et al. [25]. The solution strategy implies driving to zero the equations governing the real and imaginary parts of each mode k:

$$\frac{\partial \hat{w}_{\mathrm{Re}}}{\partial \tau} + \hat{R}_{\mathrm{Re}} - k\hat{w}_{\mathrm{Im}} = 0 \tag{18}$$

$$\frac{\partial \hat{w}_{\mathrm{Im}}}{\partial \tau} + \hat{R}_{\mathrm{Im}} + k\hat{w}_{\mathrm{Re}} = 0 \tag{19}$$

Because these equations are coupled through the source term $ik\hat{w}_k$, a fully implicit scheme would require solving them simultaneously. To preserve the simplicity of the original NLFD method, we keep this source term explicit, allowing us to solve the real and imaginary parts separately. For each cell, we write

$$\frac{\hat{w}_c^{n+1} - \hat{w}_c^n}{\Delta\tau} + \left[\hat{R}_c^{n+1} - \hat{R}_c^n\right] = -\hat{R}_c^n - ik\hat{w}_c^n \tag{20}$$

We linearize the residual, distinguishing between the cell's and the neighbor's contributions:

$$\begin{aligned}
&\frac{\hat{w}_c^{n+1} - \hat{w}_c^n}{\Delta\tau} + \frac{\partial \hat{R}_c}{\partial \hat{w}_c}\left[\hat{w}_c^{n+1} - \hat{w}_c^n\right] \\
&\quad + \sum_{nb\neq c} \frac{\partial \hat{R}_c}{\partial \hat{w}_{nb}}[\hat{w}_{nb}^{n+1} - \hat{w}_{nb}^n] = -\hat{R}_c^n - ik\hat{w}_c^n
\end{aligned} \tag{21}$$

To reduce the stencil size and memory requirements, the scheme employs a Gauss–Seidel approach in which the latest available solution is used, which allows transferring the neighbor's contribution to the right-hand side. Noting the sweep iteration as s and the latest available update as $*$, we write

$$\begin{aligned}
&\left(\frac{I}{\Delta\tau} + \frac{\partial \hat{R}_c}{\partial \hat{w}_c}\right)\left[\hat{w}_c^{n+1} - \hat{w}_c^n\right]^{s+1} \\
&\quad = -\sum_{nb\neq c} \frac{\partial \hat{R}_c}{\partial \hat{w}_{nb}}\left[\hat{w}_{nb}^{n+1} - \hat{w}_{nb}^n\right]^* - \hat{R}_c^n - ik\hat{w}_c^n
\end{aligned} \tag{22}$$

It is possible to further simplify the scheme by approximating the neighboring cell's contributions in the following fashion:

$$\hat{R}_c(w_c^n, w_{nb}^n) + \sum_{nb\neq c} \frac{\partial \hat{R}_c}{\partial \hat{w}_{nb}}\left[\hat{w}_{nb}^{n+1} - \hat{w}_{nb}^n\right]^* \approx \hat{R}_c\left(w_c^n, w_{nb}^*\right) \tag{23}$$

$$\approx \hat{R}_c(w_c^*, w_{nb}^*) - \frac{\partial \hat{R}_c}{\partial \hat{w}_c}\left[\hat{w}_c^{n+1} - \hat{w}_c^n\right]^* \tag{24}$$

$$= \hat{R}_c^* - \frac{\partial \hat{R}_c}{\partial \hat{w}_c}\left[\hat{w}_c^{n+1} - \hat{w}_c^n\right]^s \tag{25}$$

Using this approximation, the scheme simplifies to

$$\left(\frac{I}{\Delta\tau}+\frac{\partial\hat{R}_c}{\partial\hat{w}_c}\right)\left[\hat{w}_c^{n+1,s+1}-\hat{w}_c^{n+1,s}\right]$$
$$=-\left(\hat{R}_c^*+\frac{\left[\hat{w}_c^{n+1}-\hat{w}_c^n\right]^s}{\Delta\tau}+ik\hat{w}_c^n\right) \tag{26}$$

The left-hand side matrix of Eq. (26) is assembled and stored in factorized lower/upper form for the real and imaginary parts of all the modes of each cell. Using a symmetric sweeping pattern, we solve each cell sequentially by doing triangular solves until the time step is deemed sufficiently converged. Because we only require a steady-state solution to Eq. (15), partial convergence of each time step is sufficient, and thus the minimum number of sweeps that guarantees convergence are used. As noted by Fidkowski [26], solution schemes based on a local linearization of the residual can fail if a poor initial guess is used. Indeed, it is possible to predict a negative density or pressure in the early stages of the solution procedure. To prevent such nonphysical quantities, a small time increment is used for the first few iterations and is gradually increased.

In the practical implementation of this scheme, the residual in Fourier space is obtained using a pseudospectral approach. A flow period is divided in a number of n distinct time steps in which the time-dependent real-space residual is calculated. Using a discrete Fourier transform, the $(n+1)/2$ first modes of the spectral residual $\hat{R}_k^*$ are obtained and used in Eq. (26). Similarly, w is calculated from $\hat{w}_k$ by using the inverse Fourier transform. Using this pseudospectral method also considerably simplifies the computation of the scheme's Jacobian. Indeed, using the chain rule, we have

$$\frac{\partial\hat{R}}{\partial\hat{w}}=\sum_{r=1}^{n}\frac{\partial\hat{R}}{\partial R_r}\frac{\partial R_r}{\partial w_r}\frac{\partial w_r}{\partial\hat{w}} \tag{27}$$

where r denotes the time steps in real space. Moreover, noticing that $\partial\hat{R}/\partial R$ and $\partial w/\partial\hat{w}$ are simply the coefficients forming the basis functions of the forward and inverse Fourier transforms, we conclude that the spectral Jacobians are easily calculated as a linear combination of the real-space Jacobians. This method is significantly simpler than formally expressing $\hat{R}$ as a function of $\hat{w}$ and taking the appropriate derivatives.

III. Numerical Validation

A. Vortex Advection Problem

To numerically evaluate the accuracy of our SD solver, we chose to solve the vortex advection of Shu [27]. In a mean diagonal flow with parameters $(\rho,u,v,p)=(1,1,1,1)$, perturbations are added such that an isentropic vortex is created:

$$(\delta u,\delta v)=\frac{\varepsilon}{2\pi}e^{\frac{1}{2}(1-r^2)}(-\bar{y},\bar{x}) \tag{28}$$

$$\delta T=-\frac{(\gamma-1)\varepsilon^2}{8\gamma\pi^2}e^{(1-r^2)} \tag{29}$$

where $r^2=\bar{x}^2+\bar{y}^2$, $\bar{x}=x-6$, $\bar{y}=y-6$, and the vortex strength is $\varepsilon=5$.

If the domain is infinitely large, then the Euler equations admit an exact solution that is the passive advection of the original vortex along the mean flow at a mean velocity of (1,1). To replicate this condition, we solve the problem on a computational domain of $[0,14]\times[0,14]$ with periodic boundaries. The domain is discretized using five uniform structured grids of successive refinements. The coarser grids are generated from the fine grids by eliminating every other point. The numerical fluxes are evaluated using Roe's [20] Riemann solver. The simulations are integrated to $t=2$ using the five-stage Runge–Kutta scheme with a fixed time step. The time steps were made small enough to ensure time-step-independent solutions such that the spatial discretization error dominates. An example of the final solution on the coarsest grid is presented in Fig. 2. To demonstrate the accuracy of the scheme, numerical simulations are conducted and compared using the first- through fourth-order SD schemes. The rms and max density errors are computed as follows:

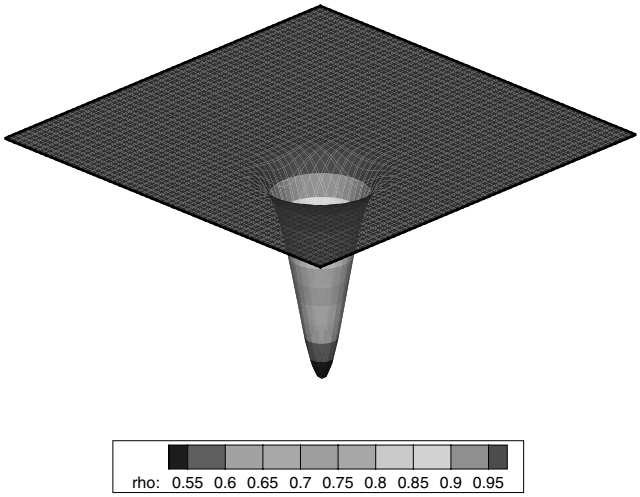

Fig. 2 Vortex advection problem: 30 × 30, third order, density profile.

$$e_{\max}=\max_i|\rho_i-\rho_{\text{exact}}| \tag{30}$$

$$e_{\text{rms}}=\left(\frac{1}{n}\sum_{i=1}^{n}|\rho_i-\rho_{\text{exact}}|^2\right)^{1/2} \tag{31}$$

The rms error in density is presented in Fig. 3 for the first- through fourth-order SD schemes. A nearly ideal order of accuracy is recovered for all simulations in both the rms and max errors, as shown in Table 1. Figure 4 also presents the measured rms error as a function of the number of degrees of freedom of the solution. For the same number of unknowns, the fourth-order SD scheme yields the lowest level of error, demonstrating the benefits of high-order formulations. The 30×30 third- and fourth-order-accurate simulations are repeated using the LU-SGS integration scheme. Figures 5 and 6 present the error as a function of the time step. For both cases, the scheme achieves its formal first-order temporal accuracy. Moreover, it also converges to a level of precision similar to the explicit simulations once the temporal error is sufficiently decayed.

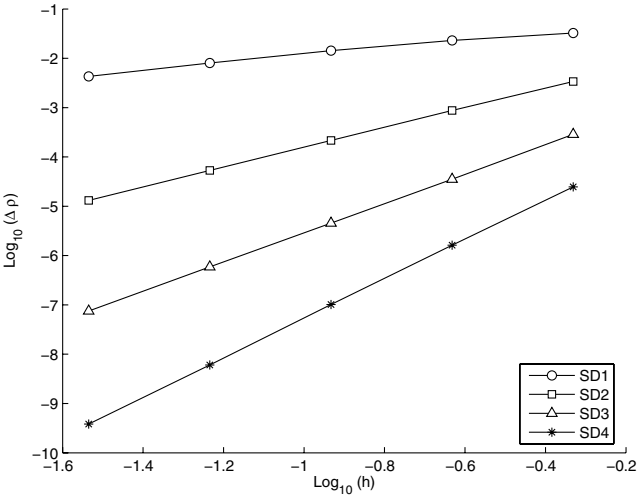

Fig. 3 Vortex advection problem: density error as a function of grid size.

Table 1 RMS and max density errors and orders of accuracy for the vortex advection problem

Order	Grid	DOF	RMS error	RMS order	Max error	Max order
1	30×30	3600	0.32597e − 01	——	0.36220e + 00	——
	60×60	14,400	0.23076e − 01	0.4983	0.25648e + 00	0.4979
	120×120	57,600	0.14263e − 01	0.6941	0.15431e + 00	0.7330
	240×240	230,400	0.80307e − 02	0.8287	0.83311e − 01	0.8893
	480×480	921,600	0.42818e − 02	0.9073	0.43273e − 01	0.9450
2	30×30	14,400	0.33752e − 02	——	0.39141e − 01	——
	60×60	57,600	0.87539e − 03	1.9470	0.10222e − 01	1.9370
	120×120	230,400	0.21616e − 03	2.0178	0.23557e − 02	2.1174
	240×240	921,600	0.53175e − 04	2.0233	0.56093e − 03	2.0703
	480×480	3,686,400	0.13163e − 04	2.0143	0.13923e − 03	2.0104
3	30×30	32,400	0.28735e − 03	——	0.46465e − 02	——
	60×60	129,600	0.35207e − 04	3.0289	0.59742e − 03	2.9593
	120×120	518,400	0.45436e − 05	2.9540	0.76179e − 04	2.9713
	240×240	2,073,600	0.58932e − 06	2.9467	0.96220e − 05	2.9850
	480×480	8,294,400	0.75185e − 07	2.9705	0.12054e − 05	2.9968
4	30×30	57,600	0.24684e − 04	——	0.43526e − 03	——
	60×60	230,400	0.16228e − 05	3.9270	0.25705e − 04	4.0818
	120×120	921,600	0.10171e − 06	3.9960	0.18959e − 05	3.7611
	240×240	3,686,400	0.60305e − 08	4.0760	0.12003e − 06	3.9814
	480×480	1,4745,600	0.38354e − 09	3.9748	0.71053e − 08	4.0784

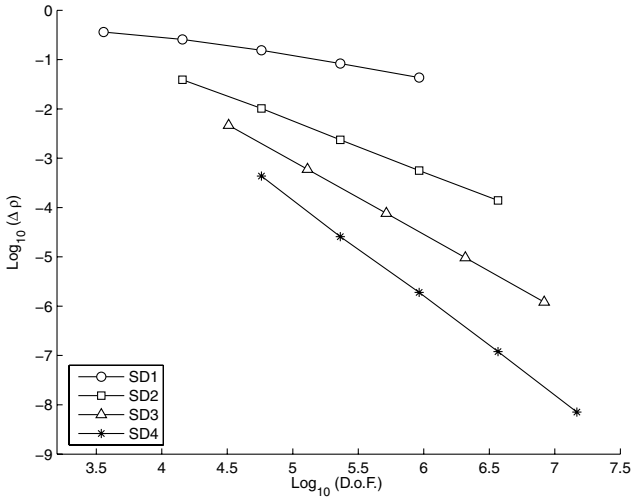

Fig. 4 Vortex advection problem: density error as a function of number of DOF

B. Subsonic NACA0012 Airfoil

In the following test, the second- through fourth-order SD schemes are used to solve the steady flow around a NACA0012 airfoil in the subsonic regime ($M_\infty = 0.5$ and $\alpha = 2\,\text{deg}$). All simulations use Roe's [20] numerical flux, a quadratic solid-wall representation, and a far-field boundary condition based on Riemann invariants with vortex correction. Meshes of sizes 128×32, 91×20 and 64×16 are used, respectively, to keep the number of degrees of freedom uniform between the three runs. The time integration is performed using the implicit LU-SGS scheme.

To numerically quantify the solution accuracy, the spurious entropy production is compared. Figure 7 presents the entropy profile along the airfoil for each solution. Although all simulations have 6.5e4 degrees of freedom (DOF), note that the high-order solutions are significantly more accurate. The average entropy levels in the domain are 9.64e − 5, 3.47e − 5, and 1.64e − 5 for the second- through fourth-order simulations. Accordingly, the third- and fourth-order schemes represent improvements by a factor of 3 and 6, respectively. The predicted drag coefficients for the three simulations are 1.6e − 4, 8e − 5, and 6e − 5. Again, these figures confirm that the high-order SD schemes are less diffusive; the spurious viscosity accounts for less than a drag count. The computed pressure contours are shown in Fig. 8. Although the second-order solution exhibits

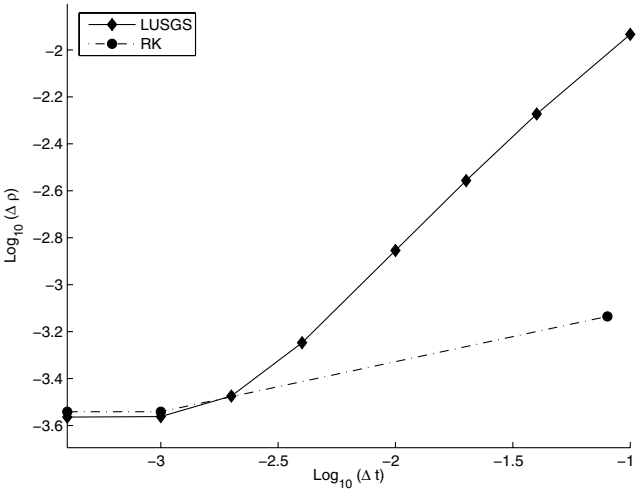

Fig. 5 Vortex advection problem: 30 × 30, third order, density error as a function of the time step.

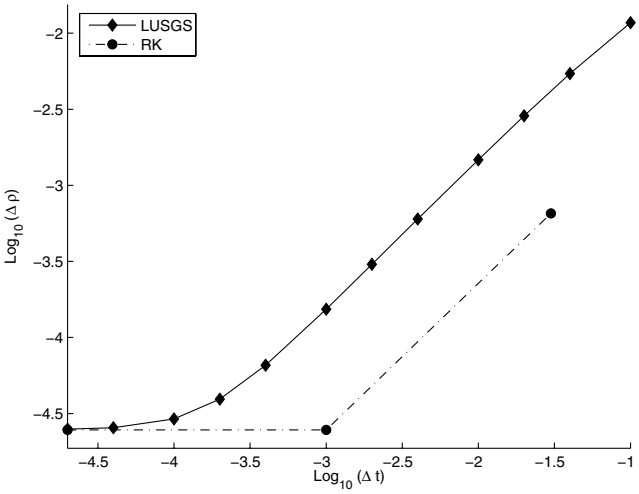

Fig. 6 Vortex advection problem: 30 × 30, fourth order, density error as a function of the time step.

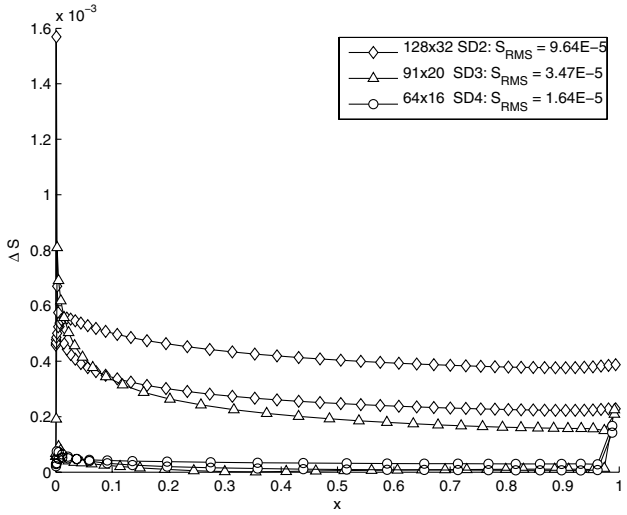

Fig. 7 NACA0012: measured entropy error against DOF

oscillations, the high-order solutions are quite smooth and well resolved.

Because this validation case possesses a steady-state solution, we will also use it to test the performance of the implicit LU-SGS time-stepping scheme. The comparison against the five-stage explicit integration scheme is done using the third-order scheme on the 128×32 grid. Figures 9a–9c display a comparison of the explicit and implicit schemes and investigate the effect of time step, number of sweeps, and the effect of freezing the Jacobian matrix. Figure 9a presents the effect of the time step on the convergence of the LU-SGS, and the number of symmetric forward and backward sweeps is kept to three. As can be observed, the implicit method is far more efficient to the explicit method and allows for a Courant–Friedrichs–Lewy (CFL) number that is 4 orders of magnitude larger and thus converges as much as 27 times faster. The effect of the number of forward and backward Gauss–Seidel sweeps is compared in Fig. 9b. The primary motivation is to reduce the number of sweeps to approximately solve each time step, thereby reducing the total computational cost while still ensuring the stability of the scheme. Figure 9b illustrates that three sweeps is the minimum allowed for this test case, and adding more sweeps slows down the computation.

Next, we explore the effect of freezing the Jacobian matrix. In Sun et al.'s [25] paper, it is reported that the performance of the LU-SGS method can be further improved by using a matrix freezing strategy. Indeed, the computation and factorization of the cells' Jacobians is a relatively costly procedure that can be bypassed by using the same matrix for multiple time steps. To this end, the Jacobians are kept frozen once the rms residual drops below 10^{-2}. Figure 9c shows the convergence rate for freezing frequencies of 0, 3, 10, and 20 time steps, in which a 17% improvement over the normal scheme is noticed. Finally, for the sake of completeness, the optimal parameters for the LU-SGS are also tested using the other SD formulations on the same grid. Figure 9d studies the effect of the order of accuracy on the convergence rate, and the rms residual is plotted against the number of iterations. The first- and second-order schemes exhibit a slightly faster convergence rate due to a higher allowable CFL number; however, both the third- and fourth-order schemes display similar rates.

IV. Demonstration Problem

The demonstration problem for the NLFD-SD scheme consists in the simulation of a pitching NACA64A010 airfoil. This case is run at a freestream Mach number of $M_\infty = 0.502$, and the pitching movement is given by

$$\alpha(t) = \alpha_m + \alpha_0 \cos(\omega t), \quad \text{about } x/c = 0.269 \tag{32}$$

where $\alpha_m = -0.22$ deg and $\alpha_o = 1.02$ deg with reduced frequency

$$\omega_r = \frac{\omega c}{2V_\infty} = 0.1$$

This corresponds to the $CT = 2$ case of Davis [28], for which the experimental results will be used to validate the scheme. Our computational grid of size 128×32 is shown in Fig. 10a. We use a quadratic boundary representation, Rusanov's [19] numerical flux, and three sweeps per time steps for the LU-SGS solver.

Using the NLFD technique, we solve the flow for a given number of modes using the third-order spatial operator. First, the simulation is performed using a single mode above the fundamental frequency on a set of progressively finer grids ranging from 32×8 to 256×64. The spatial convergence of the lift coefficient for each time instance is presented in Table 2. It can be observed that using a 128×32 grid ($\approx$6e5 DOF) ensures that each lift coefficient is well within 1% of the final values. This resolution is then considered to be sufficiently fine for engineering precision and will be used for the subsequent computations.

Figure 10b presents the lift hysteresis obtained with 1, 2, and 3 modes above the fundamental frequency. It can be seen that the three curves are nearly indistinguishable, suggesting that a single mode is sufficient to capture the lift history. This is in agreement with McMullen [23], who also demonstrated the adequacy of a single mode for smooth inviscid flow around a pitching airfoil. To further confirm the convergence of the NLFD method, the real and imaginary parts of the first mode of c_p are plotted to monitor the unsteady pressure distribution in spectral space. Figure 11 shows that the three simulations yield similar results that are in excellent agreement with Davis's [28] experimental values. The detail frame in Fig. 11b confirms that one mode captures the general pressure trend. The curves representing the 2- and 3-mode simulations are completely overlapping, proving that mode independence is achieved and that at least two modes are required to get converged pressure distributions.

To characterize the efficiency of the implicit NLFD-SD solver, the simulation using one mode is solved using the explicit five-stage Runge–Kutta (RK) method as well as the LU-SGS scheme using different parameters. Figure 12a presents the comparison between the convergence rate obtained with each integration technique. As for the steady case, the LU-SGS allows for a larger time step and thus converges about 20 times faster. However, the detail frame shows that if the time step chosen is too large, the scheme becomes unstable and the first mode diverges, which may be attributed in part to the explicit treatment of the unsteady source term in Eq. (20) of the LU-SGS scheme. Nevertheless, a significant speedup is achieved, and this restriction is deemed to be acceptable.

Further improvements are realized trough matrix freezing. Because each spectral Jacobian assembled requires calculating multiple real-space Jacobians, the gains realized are higher than those for the steady case. Figure 12b shows that those Jacobians can indeed be frozen without loss of stability or efficiency. By keeping the same matrices for three consecutive time steps, we see a 20% decrease in the computing time. Increasing the freezing frequency from 3–10 results in a total improvement of 40%, making the scheme almost 30 times faster than the explicit solution. Figure 13 presents similar comparisons for simulations using two and three modes. Once again, the LU-SGS strategy has a rate of convergence that is larger by more than an order of magnitude. All modes converge approximately at the same rate for both the explicit and implicit solvers.

Finally, we compare the convergence rate of the fundamental frequency, as shown in Fig. 14, and study the effect of increasing the number of modes. As illustrated, the convergence rates are almost identical, with a slightly lower rate for the single mode case. Similar results can be obtained using the fourth-order spectral-difference scheme together with the NLFD. Table 2 shows that even on a coarse grid, the predicted c_l values are in agreement with the fine (256×64) third-order simulations. A convergence plot for that simulation is presented in Fig. 15.

Next, the NLFD method is compared and numerically validated against a time-accurate strategy. With that intent, we repeat the third-

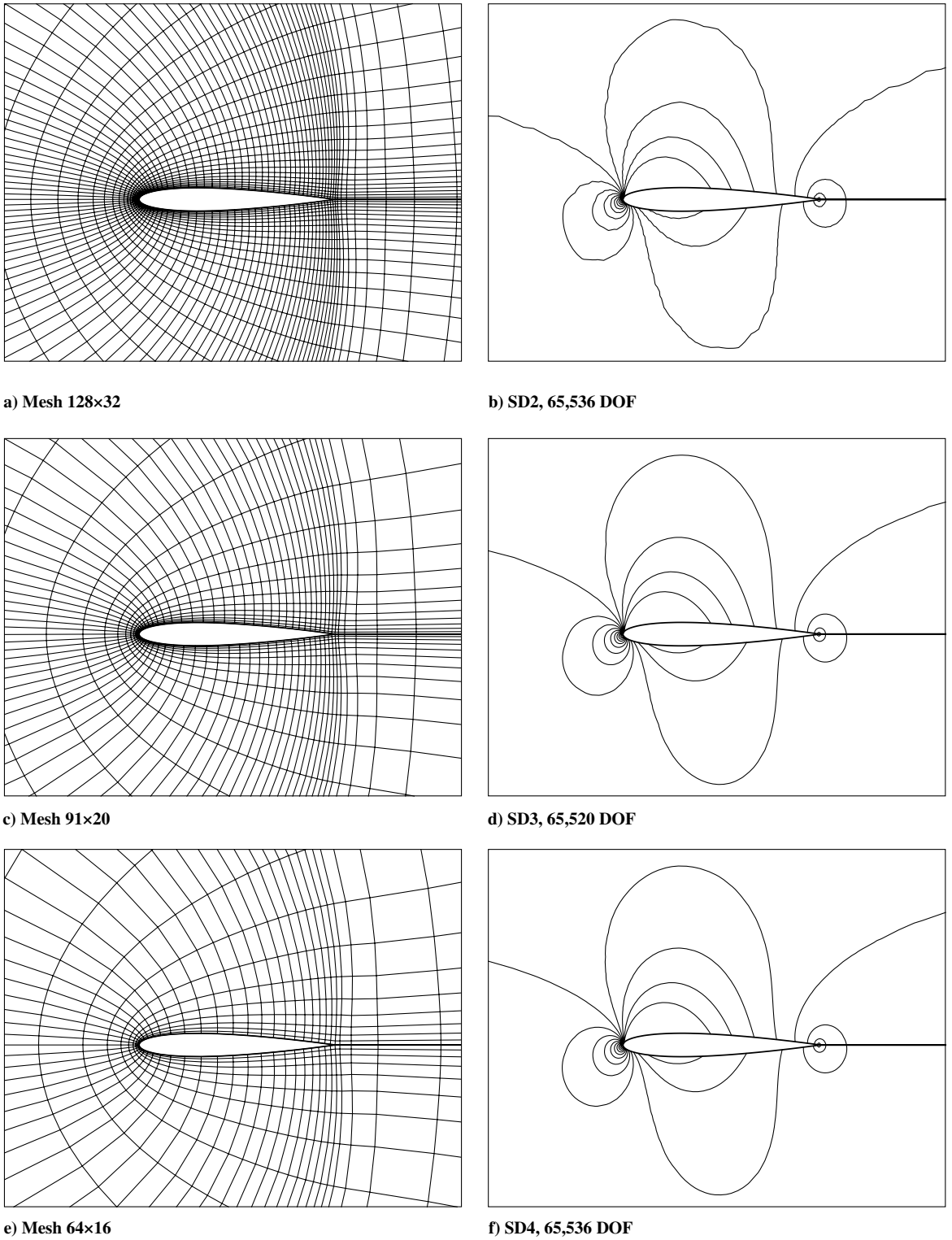

a) Mesh 128×32 **b) SD2, 65,536 DOF**

c) Mesh 91×20 **d) SD3, 65,520 DOF**

e) Mesh 64×16 **f) SD4, 65,536 DOF**

Fig. 8 Grid and pressure contours at $M_\infty = 0.5$ and $\alpha = 2\,\mathrm{deg}$ for a NACA0012 in steady flow.

order Davis [28] simulation on a 32×8 grid using a dual-time-stepping scheme (DTS). The temporal derivative of Eq. (12) is discretized using the second-order, three-point, implicit, backward-difference formula. Each time step is then treated as a steady problem and is implicitly driven to machine zero using the LU-SGS solver. The obtained lift-coefficient evolution using 1024 time steps per period is presented in Fig. 16 and compared with the NLFD results using 8 modes. A perfect qualitative agreement is obtained between the two solutions. Tables 3 and 4 presents the mean and first modes of c_l as the temporal resolution is increased. Note that the final values agree to the fifth significant digit, implying that both schemes are equivalent at convergence. To reach this convergence criterion, the NLFD needed 7 modes and required a CPU time of 2e5. The time-accurate strategy needed 1024 time steps over 7 periods, which required a CPU time of 1.6e6. On that basis, a speedup of 8 is thus reported for that test case.

As a final demonstration of the robustness of the NLFD-SD scheme, we perform the simulation on two additional reduced frequencies: $\omega_r = 0.05$ and 0.2. Figures 17a and 17c present the lift hysteresis for each of these runs. Once more, the curve representing 1, 2, and 3 modes above the fundamental frequency overlap, indicating a mode-converged simulation. For reference, the lift

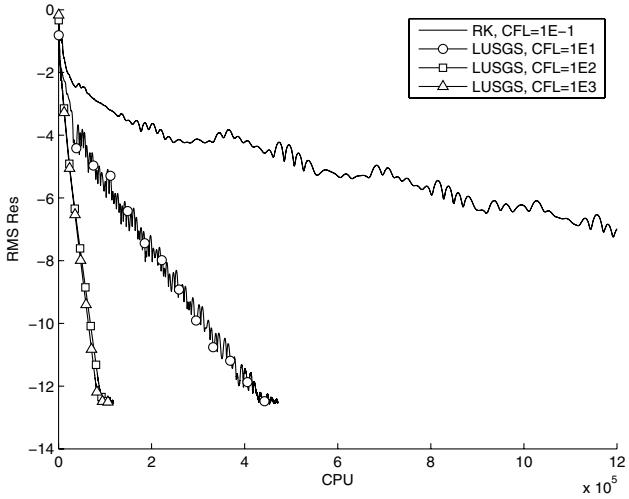

a) Effect of time step

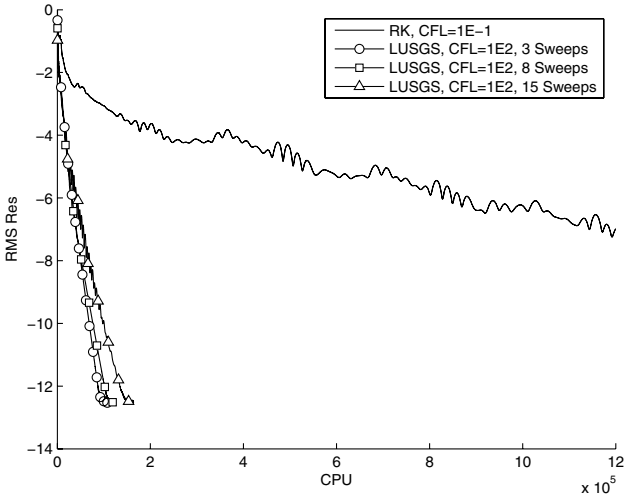

b) Effect of number of sweeps

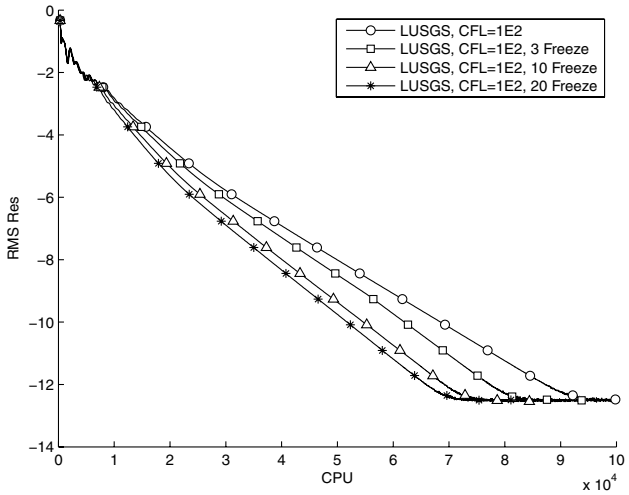

c) Effect of freezing frequency

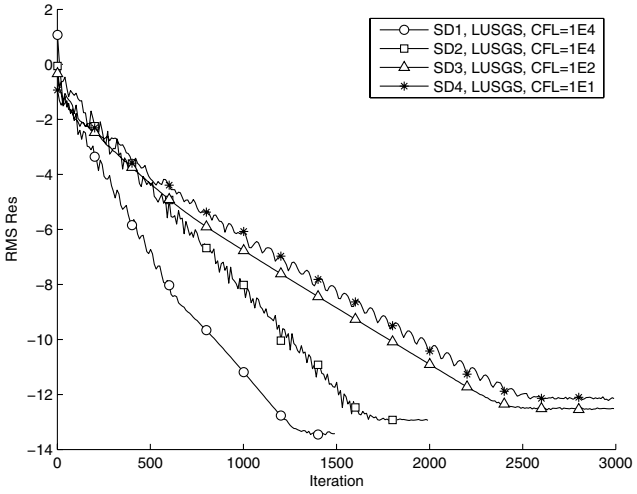

d) Effect of scheme's order

Fig. 9 Comparison between the RK and LU-SGS schemes.

hysteresis of the previous case is also presented. We observe that the increased reduced frequency induces the maximum lift produced in the flow cycle. Figures 17b and 17d illustrate the unsteady pressure distribution in spectral space. Both the real and imaginary pressure distributions confirm that one mode is sufficient; however, from the inset, at least two are required to get a converged pressure distribution. CPU run times are presented in Fig. 18a and are very comparable with Fig. 13b, illustrating the independence of the implicit solver with respect to the simulated flow condition. Figure 18b shows the convergence of the lift coefficient at several

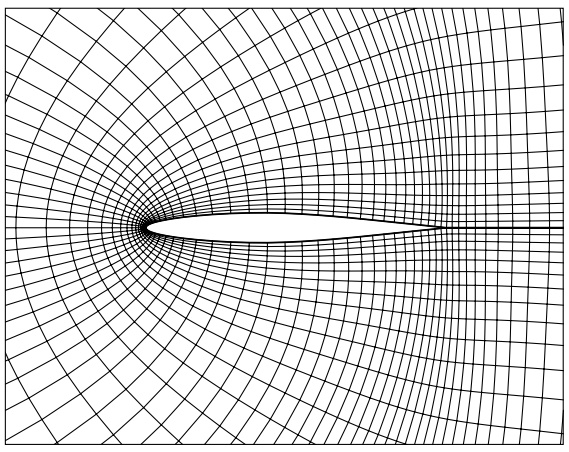

a) Mesh 128×32

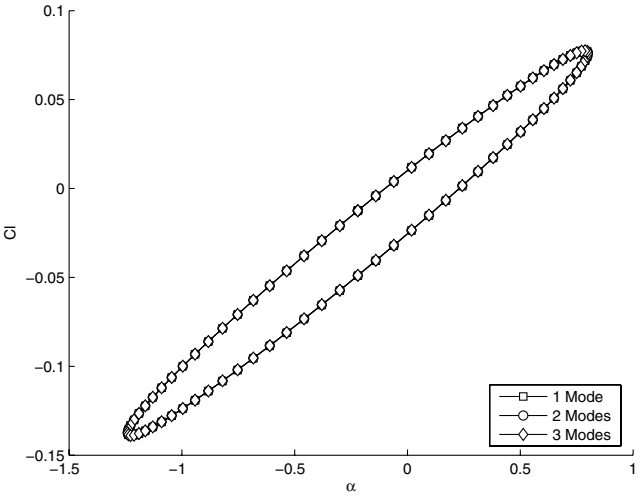

b) $C_l(\alpha)$

Fig. 10 NACA64A010: $\omega_r = 0.1$, mesh and lift hysteresis.

Table 2 Lift-coefficient convergence for the demonstration problem

			c_l		
Order	Grid	DOF	$\alpha = -0.2200$ deg	$\alpha = -1.1033$ deg	$\alpha = 0.6633$ deg
3	32×8	9216	−0.0137	−0.1278	0.0529
3	64×16	36,864	−0.0130	−0.1312	0.0526
3	128×32	147,456	−0.0124	−0.1323	0.0525
3	256×64	589,824	−0.0124	−0.1323	0.0528
4	96×24	147,456	−0.0126	−0.1324	0.0529

different time instances as a periodic steady-state flow is realized. Clearly, the c_l values of each time instance stabilize well before the residual reaches machine zero, indicating that the periodic simulation can be halted prematurely if engineering accuracy is required.

V. Conclusions

This paper presents the NLFD-SD high-order scheme for the solution of periodic inviscid flows. The high resolution in both time and space of this compact scheme is validated on different problems. The vortex advection case is demonstrated, and a near-ideal order of accuracy is recovered for the first- through fourth-order SD schemes. The simulation of a steady subsonic NACA0012 airfoil is also performed to evaluate the efficiency of the implicit LU-SGS solver. The scheme is used on a pitching NACA64A010 demonstration problem in which it is successfully validated against experimental results. It is also shown that the implicit solver with matrix freezing leads to speedups of more than an order of magnitude. Finally, a comparison between the developed approach and a time-accurate dual-time-stepping strategy is performed. It is shown that both approaches are equivalent at convergence, with the NLFD representing a speedup of 8 over the DTS method. Future work will involve testing the NLFD-SD scheme on flows with strong nonlinearities such as moving shock waves and viscous effects.

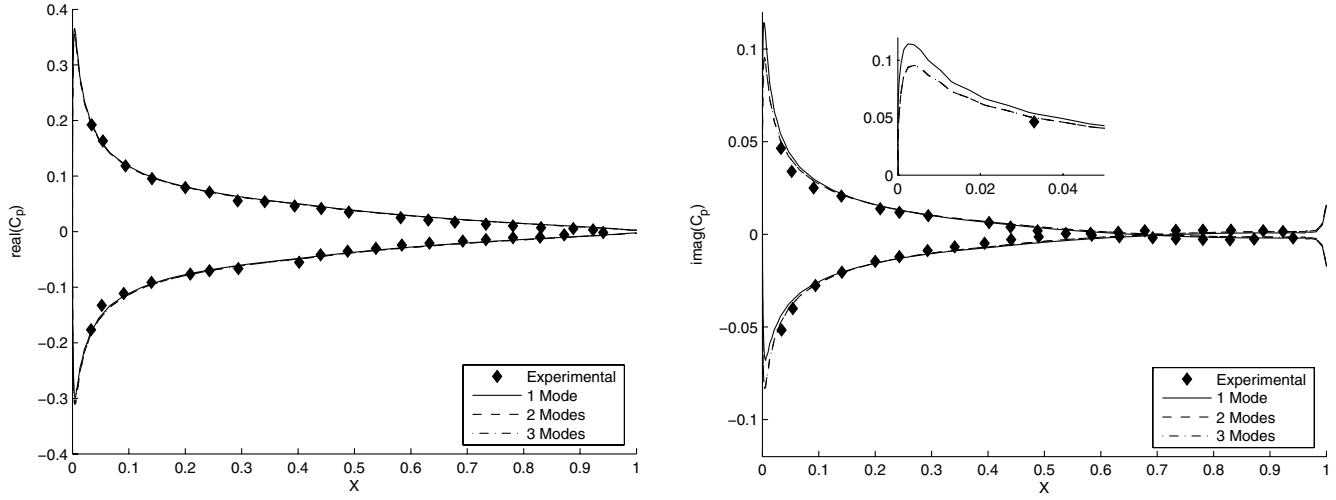

a) Re($\hat{c}_p$) **b) Im($\hat{c}_p$)**

Fig. 11 Numerical and experimental first mode of c_p.

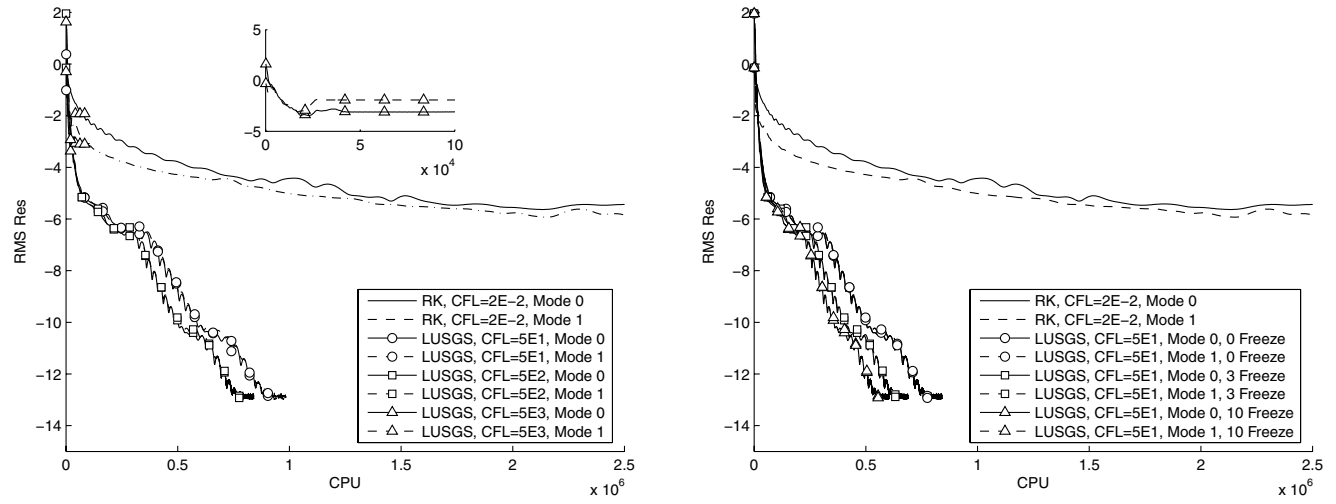

a) Effect of time step **b) Effect of matrix freezing**

Fig. 12 Comparison between the RK and LU-SGS schemes for a one-mode NLFD simulation.

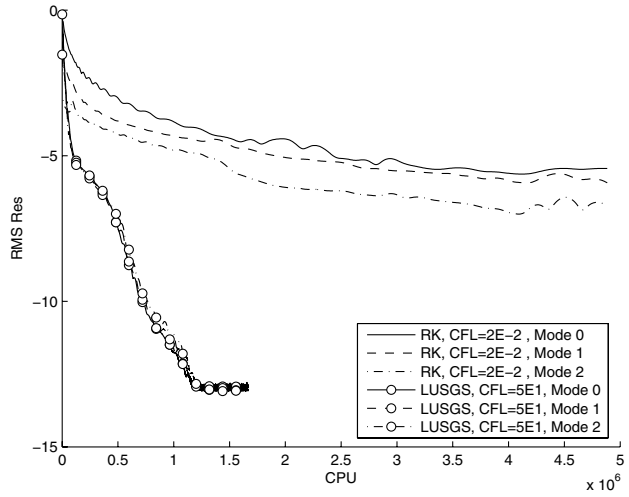

a) 2 modes

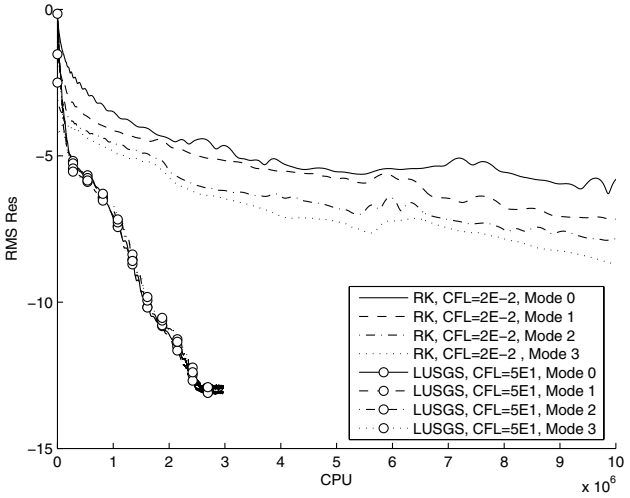

b) 3 modes

Fig. 13 Comparison between the RK and LU-SGS schemes for two and three modes NLFD simulations.

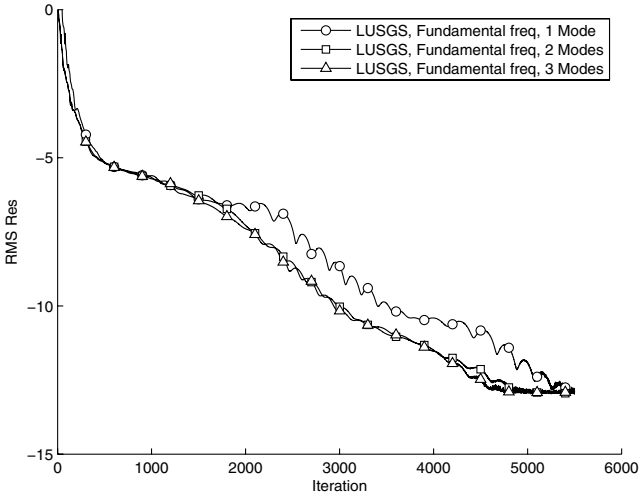

Fig. 14 Effect of the number of modes on the convergence rate of the zeroth mode, third order.

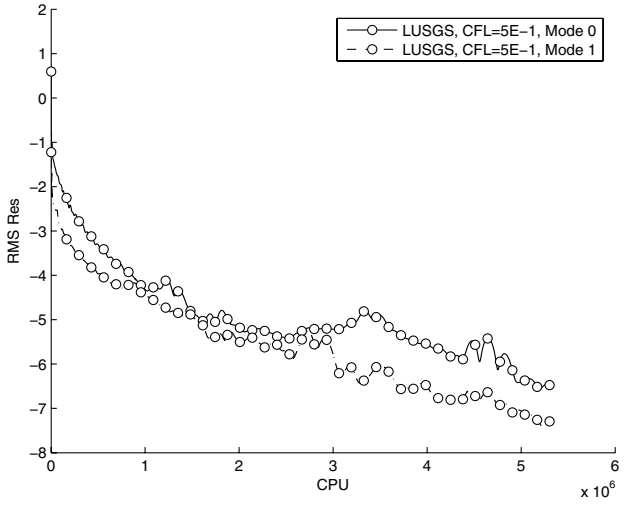

Fig. 15 Convergence of the 96 × 24, fourth-order simulation.

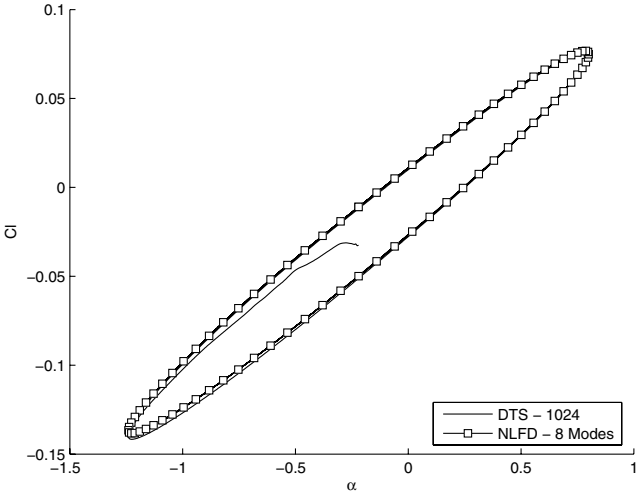

Fig. 16 Time-accurate and NLFD c_l hysteresis.

Table 3 NLFD $\bar{c}_l$ and $\hat{c}_l$

Modes	$\bar{c}_l$	$\hat{c}_l$
1	$-0.3006177e-01$	$0.9622533e-02+0.5233166e-01i$
2	$-0.3069420e-01$	$0.9699423e-02+0.5235933e-01i$
3	$-0.3065299e-01$	$0.9860353e-02+0.5271320e-01i$
4	$-0.3064547e-01$	$0.9869166e-02+0.5268716e-01i$
5	$-0.3067235e-01$	$0.9872353e-02+0.5271095e-01i$
6	$-0.3066414e-01$	$0.9873912e-02+0.5271737e-01i$
7	$-0.3066367e-01$	$0.9873386e-02+0.5271651e-01i$
8	$-0.3066368e-01$	$0.9873379e-02+0.5271649e-01i$

Table 4 Dual-time-stepping $\bar{c}_l$ and $\hat{c}_l$

Time steps	$\bar{c}_l$	$\hat{c}_l$
12	$-0.3055247e-01$	$0.9117501e-02+0.5187977e-01i$
24	$-0.3063185e-01$	$0.9692436e-02+0.5239203e-01i$
32	$-0.3065331e-01$	$0.9778853e-02+0.5251898e-01i$
48	$-0.3066665e-01$	$0.9836489e-02+0.5262420e-01i$
64	$-0.3066744e-01$	$0.9865998e-02+0.5269342e-01i$
128	$-0.3066621e-01$	$0.9869606e-02+0.5270356e-01i$
192	$-0.3066499e-01$	$0.9871778e-02+0.5271083e-01i$
256	$-0.3066446e-01$	$0.9872511e-02+0.5271332e-01i$
512	$-0.3066387e-01$	$0.9873183e-02+0.5271570e-01i$
1024	$-0.3066372e-01$	$0.9873328e-03+0.5271630e-01i$

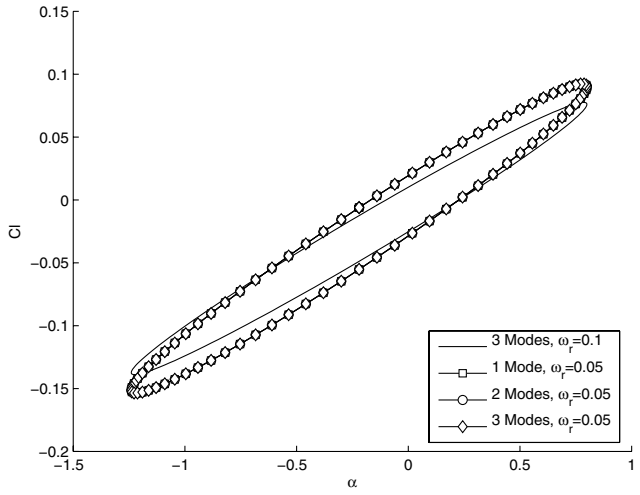

a) $c_l(\alpha)$, ω_r=0.05

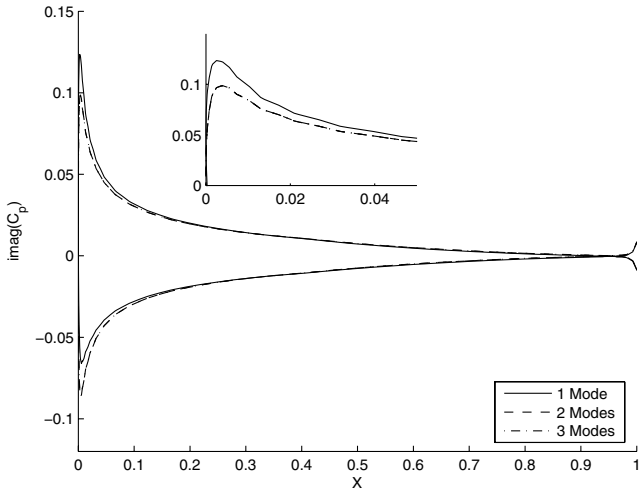

b) $\mathrm{Im}(\hat{c_p})$, ω_r=0.05

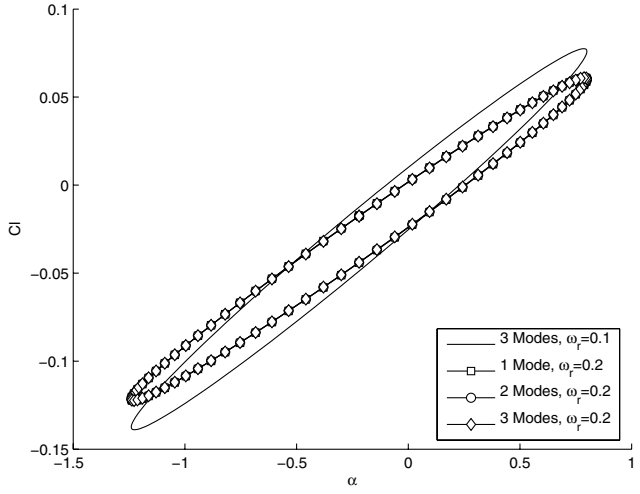

c) $c_l(\alpha)$, ω_r=0.2

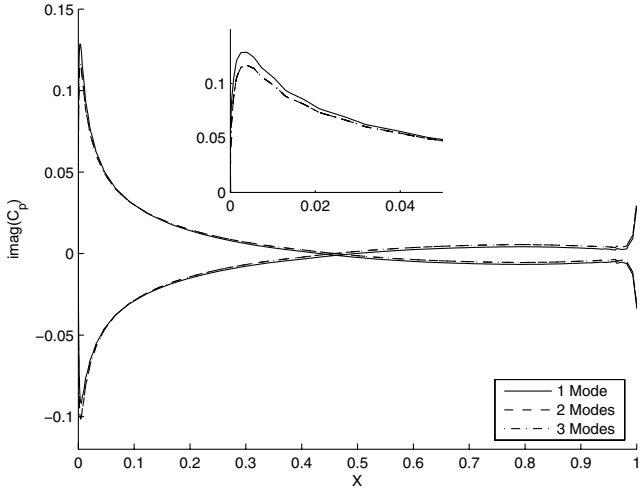

d) $\mathrm{Im}(\hat{c_p})$, ω_r=0.2

Fig. 17 NACA64A010: $\omega_r = 0.05$ and 0.2, lift hysteresis and unsteady pressure distribution.

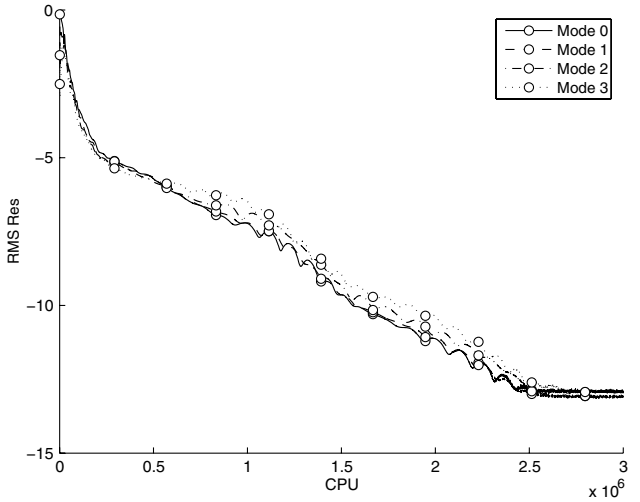

a) Convergence, 3 modes, ω_r = 0.2

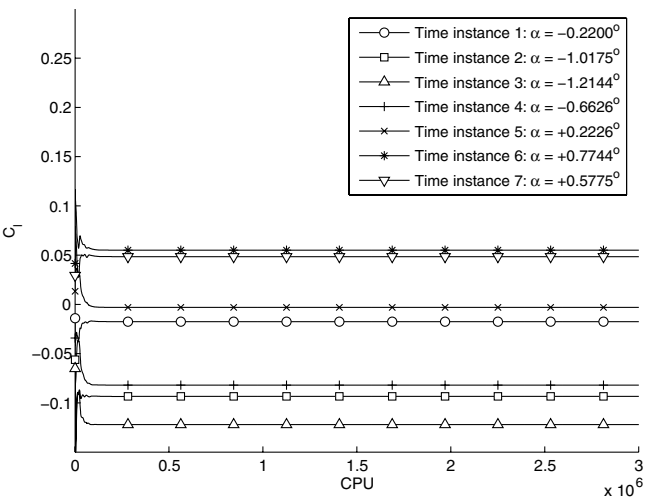

b) c_l convergence, 3 modes, ω_r = 0.2

Fig. 18 NACA64A010: $\omega_r = 0.05$ and 0.2, residual and lift convergence.

Alternative SD formulations on structured and unstructured grid will also be considered.

Acknowledgments

This research has benefited from the generous support of the Fonds de Recherche sur la Nature et les Technologies.

References

[1] Hall, K. C., Thomas, J. P., and Clark, W. S., "Computation of Unsteady Nonlinear Flows in Cascades Using a Harmonic Balance Technique," *AIAA Journal*, Vol. 40, No. 5, 2002, pp. 879–886.

[2] McMullen, M., Jameson, A., and Alonso, J., "Acceleration of Convergence to a Periodic Steady State in Turbomachinery Flows," 39th Aerospace Sciences Meeting and Exhibit, AIAA Paper 01-0152, Reno, NV, Jan. 2001.

[3] McMullen, M., Jameson, A., and Alonso, J., "Application of a Non-Linear Frequency Domain Solver to the Euler and Navier–Stokes Equations," 40th Aerospace Sciences Meeting and Exhibit, AIAA Paper 02-0120, Reno, NV, Jan. 2002.

[4] Nadarajah, S., "Convergence Studies of the Time Accurate and Non-Linear Frequency Domain Methods for Optimum Shape Design," *International Journal of Computational Fluid Dynamics*, Vol. 21, No. 5, 2007, pp. 189–207. doi:10.1080/10618560701577328

[5] Gopinath, A., and Jameson, A., "Time Spectral Method for Periodic Unsteady Computations over Two- and Three-Dimensional Bodies," 43th Aerospace Sciences Meeting and Exhibit, AIAA Paper 2005-1220, Reno, NV, Jan. 2005.

[6] Kopriva, D., and Kolias, J., "A Conservative Staggered-Grid Chebyshev Multidomain Method for Compressible Flows," *Journal of Computational Physics*, Vol. 125, No. 1, 1996, pp. 244–261. doi:10.1006/jcph.1996.0091

[7] Kopriva, D., "A Conservative Staggered-Grid Chebyshev Multidomain Method for Compressible Flows. 2: A Semi-Structured Method," *Journal of Computational Physics*, Vol. 128, No. 2, 1996, pp. 475–488. doi:10.1006/jcph.1996.0225

[8] Liu, Y., Vinokur, M., and Wang, Z. J., "Spectral Difference Method for Unstructured Grids 1: Basic Formulation," *Journal of Computational Physics*, Vol. 216, No. 2, 2006, pp. 780–801. doi:10.1016/j.jcp.2006.01.024

[9] Wang, Z., and Liu, Y., "The Spectral Difference Method for the 2-D Euler Equations on Unstructured Grids," 17th AIAA Computational Fluid Dynamics Conference, AIAA Paper 2005-5112, Toronto, June 2005.

[10] Sun, Y., Wang, Z., and Liu, Y., "High-Order Multidomain Spectral Difference Method for the Navier-Stokes Equations on Unstructured Hexahedral Grids," *Communications in Computational Physics*, Vol. 2, No. 2, 2007, pp. 310–333.

[11] May, G., and Jameson, A., "A Spectral Difference Method for the Euler and Navier–Stokes Equations on Unstructured Meshes," 44th Aerospace Sciences Meeting and Exhibit, AIAA Paper 2006-304, Reno, NV, Jan. 2006.

[12] Cockburn, B., and Shu, C.-W., "TVB Runge–Kutta Local Projection Discontinuous Galerkin Finite Element Method for Conservation Laws 2: General Framework," *Mathematics of Computation*, Vol. 52, No. 186, 1989, pp. 411–435. doi:10.2307/2008474

[13] Cockburn, B., and Shu, C.-W., "The Runge–Kutta Discontinuous Galerkin Method for Conservation Laws 5: Multidimensional Systems," *Journal of Computational Physics*, Vol. 141, No. 2, 1998, pp. 199–224. doi:10.1006/jcph.1998.5892

[14] Wang, Z., "Spectral (Finite) Volume Method for Conservation Laws on Unstructured Grids 1: Basic Formulation," *Journal of Computational Physics*, Vol. 178, No. 1, 2002, pp. 210–251. doi:10.1006/jcph.2002.7041

[15] Wang, Z., Zhang, L., and Liu, Y., "Spectral (Finite) Volume Method for Conservation Laws on Unstructured Grids 4: Extension to Two-Dimensional Systems," *Journal of Computational Physics*, Vol. 194, No. 2, 2004, pp. 716–741. doi:10.1016/j.jcp.2003.09.012

[16] Huynh, H. T., "A Flux Reconstruction Approach to High Order Schemes Including Discontinuous Galerkin Methods," *AIAA CFD Conference*, AIAA Paper 2007-4079, 2007.

[17] Van den Abeele, K., Lacor, C., and Wang, Z., "On the Connection Between the Spectral Volume and Spectral Difference Method," *Journal of Computational Physics*, Vol. 227, No. 2, 2007, pp. 877–885. doi:10.1016/j.jcp.2007.08.030

[18] Van den Abeele, K., Lacor, C., and Wang, Z., "On the Stability and Accuracy of the Spectral Difference Method," *Journal of Scientific Computing*, Vol. 37, No. 2, Nov. 2008, pp. 162–188. doi:10.1007/s10915-008-9201-0, 2008.

[19] Rusanov, V. V., "Calculation of Interaction of Non-Steady Shock Waves with Obstacles," *Computational Mathematics and Mathematical Physics*, Vol. 1, 1961, pp. 267–279.

[20] Roe, P., "Approximate Riemann Solvers, Parameter Vectors and Difference schemes," *Journal of Computational Physics*, Vol. 43, No. 2, 1981, pp. 357–372. doi:10.1016/0021-9991(81)90128-5

[21] Bassi, F., and Rebay, S., "High-Order Accurate Discontinuous Finite Element Solution of the 2-D Euler Equations," *Journal of Computational Physics*, Vol. 138, No. 2, 1997, pp. 251–285. doi:10.1006/jcph.1997.5454

[22] Wang, Z., and Liu, Y., "Extension of the Spectral Volume Method to High-Order Boundary Representation," *Journal of Computational Physics*, Vol. 211, No. 1, 2006, pp. 154–178. doi:10.1016/j.jcp.2005.05.022

[23] McMullen, M., "The Application of a Non-Linear Frequency Domain Solver to the Euler and Navier–Stokes Equations," Ph.D. Thesis, Dept. of Aeronautics and Astronautics, Stanford Univ., Stanford, CA, Mar. 2003.

[24] Swanson, R., and Turkel, E., "Multistage Schemes with Multigrid for Euler and Navier-Stokes Equations—Components and Analysis," NASA TP 3631, Aug. 1997.

[25] Sun, Y., Wang, Z., Liu, Y., and Chen, C., "Efficient Implicit LU-SGS Algorithm for High-Order Spectral Difference Method on Unstructured Hexahedral Grids," 45th Aerospace Sciences Meeting and Exhibit, AIAA Paper 2007-0313, Reno, NV, Jan. 2007.

[26] Fidkwoski, K., "A High-Order Discontinuous Galerkin Multigird Solver for Aerodynamic Applications," M.S. Thesis, Dept. of Aeronautics and Astronautics, Massachusetts Inst. of Technology, Cambridge, MA, June 2004.

[27] Shu, C.-W., *Essentially Non-Oscillatory and Weighted Essentially Non-Oscillatory Schemes for Hyperbolic Conservation Laws*, Lecture Notes in Mathematics, Vol. 1697, Springer–Verlag, Berlin, 1998, p. 325.

[28] Davis, S., "NACA 64A101 (NASA Ames model) Oscillatory Pitching," AGARD Rept. 702, Neuilly-sur-Seine, France, Jan. 1982.

Z. Wang
Associate Editor